Consistency of Measurements of Wavelength Position From Hyperspectral Imagery: Use of the Ferric Iron Crystal Field Absorption at ~900 nm as an Indicator of Mineralogy

Richard J. Murphy, *Member, IEEE*, Sven Schneider, and Sildomar T. Monteiro, *Member, IEEE*

Abstract—Several environmental and sensor effects make the determination of the wavelength position of absorption features in the visible near infrared (VNIR) (400–1200 nm) from hyperspectral imagery more difficult than from nonimaging spectrometers. To evaluate this, we focus on the ferric iron crystal field absorption, located at about 900 nm (F_{900}), because it is impacted by both environmental and sensor effects. The consistency with which the wavelength position of F_{900} can be determined from imagery acquired in laboratory and field settings is evaluated under artificial and natural illumination, respectively. The wavelength position of F_{900}, determined from laboratory imagery, is also evaluated as an indicator of the proportion of goethite in mixtures of crushed rock. Results are compared with those from a high-resolution field spectrometer. Images describing the wavelength position of F_{900} showed large amounts of spatial variability and contained an artifact—a consistent shift in the wavelength position of F_{900} to longer wavelengths. These effects were greatly reduced or removed when wavelength position was determined from a polynomial fit to the data, enabling wavelength position to be used to map hematite and goethite in samples of ore and on a vertical surface (a mine face). The wavelength position of F_{900} from a polynomial fit was strongly positively correlated with the proportion of goethite ($R^2 = 0.97$). Taken together, these findings indicate that the wavelength position of absorption features from VNIR imagery should be determined from a polynomial (or equivalent) fit to the original data and not from the original data themselves.

Index Terms—Geology, hyperspectral sensors, image classification, infrared spectroscopy, minerals, mining industry, polynomials, remote sensing, signal processing, spectral analysis, terrain mapping.

I. INTRODUCTION

FOR nearly three decades, imaging spectrometers have been used to acquire information about the geology and mineralogy of the Earth's surface [1]. During this time, new analytical approaches have been developed to identify and map minerals in hyperspectral imagery by matching their spectral
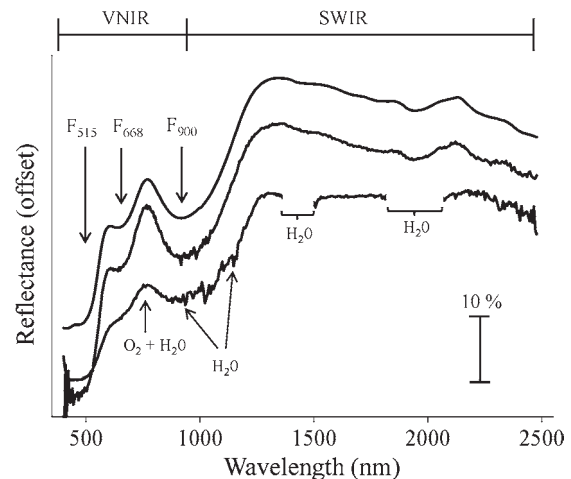
Fig. 1. Spectra of goethite measured using an ASD spectrometer (top), single image pixel spectra measured in the laboratory and under natural sunlight (middle and bottom, respectively). Spectra are offset on the vertical axis for clarity (scale showing 10% reflectance indicated at lower right). Absorption features caused by crystal field effects (F_{515}, F_{668}, and F_{900}) are indicated. Wavelengths affected by atmospheric absorption are shown on the bottom spectrum. The spectral regions sensed by the separate VNIR and SWIR imaging sensors are shown above the graph.

curves to libraries of known minerals, reviewed by Plaza *et al.* [2] and Cloutis [3]. Many established techniques such as the spectral angle mapper (SAM) and spectral unmixing exploit the full dimensionality of the data [4]–[7]. There remains, however, a need to extract pertinent features from spectra such as the wavelength position of absorption features. Wavelength position provides information about the identity of absorbing minerals as well as aspects of their geochemistry such as the degree of cation substitution [8]–[10]. The ability to reliably extract information on wavelength position depends upon the amount of noise in the spectrum and the location of the absorption feature in the spectral curve. Determining the wavelength position of features in the short-wave infrared (SWIR) is relatively straightforward because the features are intense and relatively narrow [11]–[13]. In the visible near infrared (VNIR), the accurate determination of wavelength position is more challenging. Many features, such as those of ferric iron, are broader and are located in a region of the spectrum affected by intense atmospheric absorptions (see Fig. 1). This may, at

This article has been accepted for inclusion in a future issue of this journal. Content is final as presented, with the exception of pagination.

2   IEEE TRANSACTIONS ON GEOSCIENCE AND REMOTE SENSING

TABLE I
WAVELENGTH POSITION OF F_{900} FOR HEMATITE AND GOETHITE REPORTED BY VARIOUS STUDIES

Reference	Hematite	Goethite	Material
Haest et al. 2012 [15]	890	960	Drill chips
Cudahy & Ramanaidou 1997 [17]	857 - 870	913 - 931	Synthetic and natural
Townsend 1987 [33]	855	925	Regolith
Morris et al. 1985 [9]	846 - 870	908 – 932	Commercial products
Buckingham and Sommer 1983 [34]	866 - 877	895 - 934	Rock and soil

Note that comparisons of the wavelength position of F_{900} among studies cannot be made unless the continuum has been removed over the same wavelength regions (i.e. the regions have the same wavelengths for end points). Therefore, only the findings of Haest et al. (2012) are directly comparable to the findings presented in this study.

least partly, explain why the vast majority of studies which have used wavelength position as a feature in the study of iron oxides have been done in the laboratory using artificial light [9], [14]–[16], with the exception of the work by Cudahy and Ramanaidou [17] who extended their laboratory study into the field.

All of the aforementioned studies used data from nonimaging spectrometers which have a high spectral resolution and bit depth, producing relatively clean spectra across the VNIR with a large signal-to-noise ratio. The determination of wavelength position is more difficult from hyperspectral imaging sensors than from nonimaging sensors for several reasons: 1) Data are noisier, particularly toward the beginning and end of the sensed spectral range (e.g., > 930 nm for VNIR sensors [18]); 2) bandpasses are typically broader than their nonimaging counterparts; and 3) physically separate sensors are required to acquire imagery in the VNIR (400 to ∼970 nm) and SWIR (∼970–2450 nm) parts of the spectrum. Residual errors in calibration and in the spatial registration of images acquired by the separate VNIR and SWIR sensors can introduce an offset in reflectance in spectra at the crossover point between the sensors. Major absorption features of some minerals (e.g., those containing ferric iron) are located within a spectral region sensed by both VNIR and SWIR imagers, i.e., they straddle sensor boundaries. These combined effects present a significant impediment to determining the true wavelength position of VNIR features from imagery. To date, however, no published studies have assessed the accuracy and consistency with which wavelength position can be determined from hyperspectral imagery for absorption features in the VNIR (400–1200 nm). To address this, we have selected the crystal field absorption of ferric iron located at ∼900 nm (F_{900}). This feature was selected because it is affected by all the aforementioned factors and thus presents a difficult test of our ability to determine its wavelength position from imagery (see Fig. 1).

In addition to F_{900}, the VNIR spectra of iron oxides show strong absorptions centered at ∼515 nm and ∼668 nm, also caused by crystal field effects. These crystal field features have different intensities for hematite and goethite, with the strength of the feature at 668 nm increasing with increasing proportion of goethite [19]. The wavelength position of F_{900} is of particular importance because it has been related to the proportion of goethite ($FeOOH$) relative to hematite (Fe_2O_3)

in samples of iron ore [15], [17]. Increasing the amounts of goethite relative to hematite causes the wavelength position of F_{900} to shift to longer wavelengths (see Table I). It should be stressed, however, that comparisons of wavelength position among studies cannot be made unless the removal of the spectral continuum—a prerequisite to the determination of wavelength position—has been done over the same wavelength range. Detecting this shift is of major significance to mining companies. To automate and guide the mining process and to determine the type of ore, mining companies require information on the relative amounts of hematite and goethite on mine faces (using natural sunlight) and in crushed ore on conveyor belts (using artificial light). Hyperspectral imagery is ideally suited to this task, yet there remains the uncertainty about the consistency with which wavelength position can be identified using these different types of illumination. Using hyperspectral imagery acquired under artificial light, we test the accuracy and consistency with which the wavelength position of F_{900} can be determined from samples of compositionally homogeneous rock powders and from topographically complex "whole rock" samples of iron ore. We then test the hypothesis that wavelength position can be determined from hyperspectral imagery with sufficient accuracy as to estimate the proportion of goethite in artificial mixtures of crushed rock. Because these experiments are done in the laboratory under controlled conditions, without the effects of the intervening atmosphere, they represent the best case scenario for determining the wavelength position of F_{900} from hyperspectral imagery. We then apply the same methods to determine wavelength position from imagery of an open-pit mine in the Pilbara, Western Australia. This presented a more difficult test for determining wavelength position as data are acquired using natural sunlight which is affected by intense atmospheric absorption. Large variations in the brightness of hematite (with low reflectance) and goethite (with high reflectance) further increase noise in the data because the maximal sensor integration time with which data are acquired is constrained by the saturation point of the brightest pixels in the image. Spectra of pixels with darker minerals (e.g., hematite) have therefore a smaller signal-to-noise ratio. Although imagery of hematite and goethite acquired in the laboratory is affected by the same problem, data acquired in the field have additional noise caused by atmospheric absorption.

II. Materials and Methods

A. Spectrometry

To provide high-quality measurements of reflectance and a standard against which image spectra could be compared, a field spectrometer was used to acquire measurements of reflectance (350–2500 nm). The spectrometer [Analytical Spectral Devices (ASD), Boulder, CO, USA] was fitted with a reflectance probe with a high-intensity integrated light source. Reflectance spectra were acquired by taking a measurement of a calibration panel ($\sim$99% Spectralon; Labsphere, North Sutton, NH, USA) and then the target. In each case, the probe measuring window (2 cm in diameter) was placed in direct contact with the surface being measured. Forty individual spectra were averaged to produce each recorded reflectance spectrum. In the laboratory, spectra were processed to absolute reflectance by dividing by the reflectance of the calibration panel. Visual inspection of spectra indicated that they were of very high quality, with almost no noise between 400 and 2400 nm. To remove any noise that was present, a polynomial filter was applied to the data with a 100-nm window [20]. The smoothing process preserved entirely the dynamic range and shape of the original spectra. Spectra acquired in this way are henceforth termed as ASD spectra.

B. Imaging Spectrometry

The imaging system (Specim, Finland) comprised a VNIR sensor (400–970 nm) and a SWIR sensor (970–2500 nm). The former is configured to record 125 bands at an average full-width at half-maximum (FWHM) of 4.63 nm, and the latter is configured to record 246 bands at an average FWHM of 6.23 nm. The sensors were configured to have the same pixel dimensions to facilitate the spatial registration of VNIR and SWIR imagery.

1) Laboratory Imagery: The imaging sensors were mounted onto a scanning frame at a nominal distance from the target of 730 mm. Samples were placed on a table moving linearly beneath the sensors. The speed of the table was adjusted so that the correct shape of the samples was preserved in the image. The source of illumination was two arrays of seven halogen lights each. The lights were positioned to illuminate the target from both sides of the scanning frame. A calibration panel ($\sim$99%) measuring 30 cm $\times$ 3 cm was placed at one end of the scanning table. Calibration measurements were acquired separately for each sensor. The field of view of each sensor was positioned into the center of the calibration panel, and $\sim$300 frames of data were acquired without moving the linear scanning tray. The integration time was set so that spectra over the calibration did not saturate. The integration times for the measurement of the calibration panel and the target were kept constant as we wished to emulate conditions in the field, where the calibration panel and target were acquired in the same image (i.e., with the same integration time).

After acquisition, the dark current was removed from the images on a line-by-line basis. Each pixel spectrum in the VNIR image was corrected for an artifact—an increase in sensor counts toward shorter wavelengths, caused by the buildup of charge in the detector array. Calibration to reflectance was done on a line-by-line basis to remove variations in illumination across the spatial dimension of the sensor array. The VNIR and SWIR images were spatially registered using a simple shifting of one image relative to the other to account for differences in the position of the sensors on the scanning frame. VNIR and SWIR images of the same dimensions were then combined into a unified data cube. Smile and keystone effects for the imaging sensors have been quantified at less than 20% of the pixel size and were not observed in any of the processed imagery.

2) Field Imagery: Open-pit mines in Western Australia are arduous environments for the collection for hyperspectral data. Sensors and computer equipment have to be protected against high ambient temperatures ($> 50\,^{\circ}$C), direct sunlight, and dust. This was done by enclosing both sensors in an air-conditioned box, with the lens of the sensors protruding through. Cool, filtered, desiccated air was pumped into the top of the box and exhausted through the bottom. The entire enclosure was mounted on a rotating stage to acquire the image.

Reflectance standards of various brightness (Spectralon; with nominal reflectances of 15%, 30%, 40%, and 100%) were placed within the field of view of the imaging sensor. The orientation of the panels was adjusted to match the orientation of the slope of the mine face. For this present study, an integration time was selected for each sensor so that pixel values over the 30% calibration panel or the mine face did not saturate. Data were processed as described for the laboratory imagery but were calibrated to reflectance on a band-by-band basis using the average value of pixels over the calibration panel. A mask was applied to the image to remove pixels which contained signatures of live or dead vegetation (as in [21]).

C. Validation of Wavelength Calibration of Sensors

To check the wavelength calibration of the ASD field spectrometer and the Specim imaging sensors, spectra were acquired from a Spectralon calibration standard, doped with the rare-earth metal holmium. The holmium standard was calibrated to a National Laboratory Traceable Standard by the manufacturer (Labsphere, North Sutton, NH, USA). The calibration certificate provided by the manufacturer listed several intense sharp features in the VNIR region and one in the SWIR. Measurements were made of the holmium standard by the ASD spectrometer and imaging sensors. In each case, measurements were made relative to pure $\sim$99%-reflective Spectralon and converted to absolute reflectance units. Replicate spectra acquired by the ASD field spectrometer were averaged ($n = 8$). VNIR and SWIR images were acquired from the panel and an average spectrum calculated from the pixels from the center of the holmium standard. The known wavelength positions of the absorption features of the holmium standard provided by the manufacturer were then subtracted from those measured by the ASD spectrometer and Specim imagers, respectively (see Table II).

For the ASD spectrometer, differences in wavelength position between the known and measured wavelengths were small (< 1 nm) for the majority of features. The largest difference (2.91 nm) occurred in feature number 9. Similar results were

TABLE II
COMPARISON OF THE WAVELENGTH POSITIONS (IN NANOMETERS) OF KNOWN ABSORPTION BANDS OF HOLMIUM OXIDE WITH THOSE MEASURED
FROM A CALIBRATED HOLMIUM STANDARD BY THE ASD FIELD SPECTROMETER AND THE SPECIM IMAGING SENSORS

Band	Holmium standard	ASD	Specim imager(s)	Δ ASD	Δ Specim imager(s)
1	360.66	361	-	0.34	-
2	382.82	384	-	1.18	-
3	448.45	449	449	0.55	0.55
4	462.17	461	462	-1.17	-0.17
5	483.22	484	484	0.78	0.78
6	538.29	538	538	-0.29	-0.29
7	641.49	642	**644**	0.51	**-1.07**
8	648.65	648	**644**	-0.65	**-1.07**
9	1201.91	1199	1198	-2.91	-3.91

The differences in wavelength position between the wavelengths measured by each sensor and the calibrated wavelengths of the standard are shown in the columns Δ ASD and Δ Specim imager (s). Absorption bands 7 and 8 (an absorption doublet) are resolved as separate features by the ASD spectrometer but not the VNIR Specim imager. In the image spectra, the absorption is a singlet (shown in bold) with a wavelength position close to the midpoint between bands 7 and 8 (i.e. 645.07 nm) in the holmium standard. Thus, the value in the corresponding Δ Specim imager (s) column is the difference between these values.

found for the imaging sensors with the majority of features having a difference of < 1 nm. Again, the largest difference (3.91 nm) was found for feature number 9. Because of the broader bandpasses of the imaging sensors, image spectra did not exhibit all absorption features found in the ASD spectra. Features 7 and 8 were resolved as an absorption doublet in the ASD spectra, but in the image spectra, they were convolved into a single feature, with a minimum at 644 nm. This wavelength was close to the midpoint between bands 7 and 8 (see Table II). These data indicate that the wavelength calibrations of the ASD spectrometer and the imaging sensors are consistent. The difference between the known absorptions of holmium and those measured with the ASD spectrometer and imaging sensors is sufficiently small to allow the direct comparison of data—in this case, the wavelength position of F_{900}—for the purposes of this study.

D. Determination of Wavelength Position of F_{900}

Because the smoothed ASD spectra had small amounts of noise, the wavelength position of F_{900} was determined directly from the spectral data themselves, after normalizing the spectra for brightness by removing the spectral continuum [22]. It is not possible to define a "true" continuum for iron minerals in the VNIR because this part of the spectrum is affected by an intense charge transfer absorption which extends from the UV–visible boundary into the SWIR, across the F_{900}. F_{900} was isolated by removing the continuum between 770 and 1150 nm (see Fig. 2(a); cf. [13]). The wavelength position of F_{900} was then determined as the wavelength of minimum reflectance between 770 and 1150 nm.

In spectra where noise is present, the determination of wavelength position is more difficult. Even small amounts of noise can potentially cause large changes in wavelength position, particularly where features are broad (as is the case for F_{900}). Noise over the wavelength range of F_{900} is caused by absorption by atmospheric water vapor and/or the reduced sensitivity of the VNIR sensor (i.e., at wavelengths > 930 nm; see Fig. 1). Using data acquired in the laboratory, Haest et al. [15] reduced the impact of noise by fitting a fourth-order polynomial to all

data points in the absorption feature; the continuum was then removed from the fitted polynomial curve instead of the original spectrum. This approach is tested here on the image spectra of powdered hematite and goethite. Fourth- and fifth-order polynomials were generated from a least squares fit to the original data between 770 and 1150 nm [see Fig. 2(a)]. Initial results showed that a fifth-degree polynomial provided the best fit to the spectral curve and was better at estimating the wavelength position of F_{900} (see Section III-A). For all imagery, the wavelength position of F_{900} was determined from the original image data and, separately, from a fifth-order polynomial curve fitted to the same data. For each method, a grayscale image with the same spatial dimensions as the hyperspectral data cube was created describing the wavelength position of F_{900} at each pixel.

E. Experiments

1) Experiment 1—Consistency of Wavelength Position of F_{900} in Homogeneous Samples: Experiment 1 was designed to test how much variability occurs in the wavelength position of F_{900} derived from hyperspectral imagery of pressed homogeneous rock powders. The hypothesis was that, because powders are compositionally homogeneous, there should be little or no within-sample variability in the wavelength position of F_{900}. If large variability in wavelength position was found in imagery obtained from homogeneous powders in "ideal" laboratory conditions, then it would be unlikely that wavelength position could be determined reliably from imagery of whole rocks in the laboratory or in the field. Results were compared with those from ASD spectra.

Four rock types which had different characteristic intensities of absorption were selected for analysis: hematite, goethite, banded iron formation (BIF), and shale. Shale was selected because it had a less intense (deep) F_{900} absorption than the other rock types. This allowed the consistency of wavelength position to be tested across a range of F_{900} intensities from weak (shale) to strong (goethite). Rocks of each type were sampled from cores obtained during exploration drilling. Four replicate samples were acquired for each rock type and were separately ground to a homogeneous powder in a ring mill.
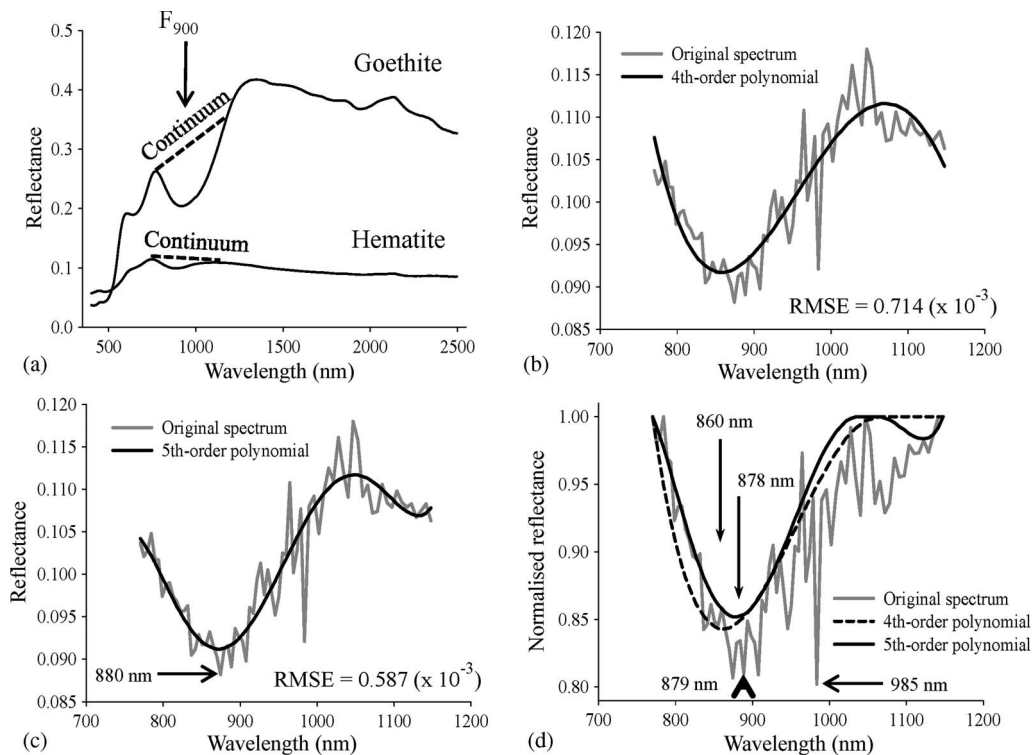
This article has been accepted for inclusion in a future issue of this journal. Content is final as presented, with the exception of pagination.

MURPHY *et al.*: CONSISTENCY OF MEASUREMENTS OF WAVELENGTH POSITION FROM HYPERSPECTRAL IMAGERY

5

Fig. 2. Effects of fitting a polynomial curve to the F_{900} absorption feature to determine its wavelength position. (a) Reflectance spectra (400–2500 nm) of hematite and goethite showing the location of the F_{900} crystal field absorption (arrow). The dashed lines represent the continuum (770–1150 nm). (b) Reflectance spectrum (770–1150 nm) of hematite with fitted fourth-order polynomial. (c) Reflectance spectrum (770–1150 nm) of hematite with fitted fifth-order polynomial. (d) Continuum-removed or normalized reflectance spectra of hematite from the original data and the fourth- and fifth-order polynomials derived therefrom. Wavelength positions of F_{900} derived from the fourth- and fifth-order polynomials are indicated (860 and 878 nm, respectively). The "true" wavelength position of F_{900} (879 nm) derived from ASD spectra is indicated by the bold arrow at the bottom. RMSE between the original spectrum and the fourth- and fifth-order polynomials is shown in (b) and (c), respectively. The wavelength position of F_{900} (i.e., the wavelength of smallest reflectance value) in the original spectrum before and after continuum removal is indicated by the horizontal arrows in (c) and (d), respectively.

Subsamples were taken to confirm the composition of the rock powder using X-ray diffraction (XRD) and X-ray fluorescence analyses. The remaining rock powder was placed on separate matt-black paper trays to a height of 1.5 cm. ASD spectra were acquired from each sample. Samples were then remixed in their trays and pressed for 10 s using a flat object of consistent weight to remove variations in the surface topography of the powder. Hyperspectral imagery was acquired of all samples using artificial light. Pixel values from the grayscale images of wavelength position were extracted for the whole area of each sample.

2) Experiment 2— Consistency of Wavelength Position of F_{900} in Whole-Rock Samples: Experiment 1 examined the ability of hyperspectral imagery to resolve the wavelength position of F_{900} from homogeneous rock powders. In reality, however, hematite and goethite often occur in discrete patches on rocks of variable shape, size, and surface topography. In Experiment 2, we determined if changes in wavelength position could be detected and mapped in whole-rock samples of iron ore. The rock samples selected for this analysis were mainly composed of discrete patches of hematite and goethite, although mixtures of the two minerals were present in some small areas. Hyperspectral imagery was acquired in the laboratory, under artificial light, and therefore presented the "best case scenario" for quantifying the wavelength position of F_{900} in whole rocks. If there was little or no agreement between the observed distribution and that mapped by F_{900}, then detect-

TABLE III
ARTIFICIAL MIXTURES OF CRUSHED ROCK WITH VARIOUS PROPORTIONS OF GOETHITE (EXPERIMENT 3)

	Quantitative XRD analysis		
Sample	Hematite (%)	Goethite (%)	Prop. Goethite
1	15	13	0.46
2	14	13	0.48
3	14	15	0.52
4	12	19	0.61
5	8	25	0.75
6	2	26	0.84

The proportion of goethite is calculated from the quantitative XRD data as wt% goethite / (wt% goethite + wt% hematite).

ing similar changes in wavelength position from hyperspectral data acquired using natural sunlight would be difficult or impossible.

To determine if the wavelength position of F_{900} derived from hyperspectral imagery was consistent with patterns of hematite and goethite on the rock surface, the distribution of pixels representing the wavelength position was compared with their visual-based distributions. While the rocks were still on the imaging platform, areas on the rock surface that were composed entirely either of hematite or goethite were identified by visual
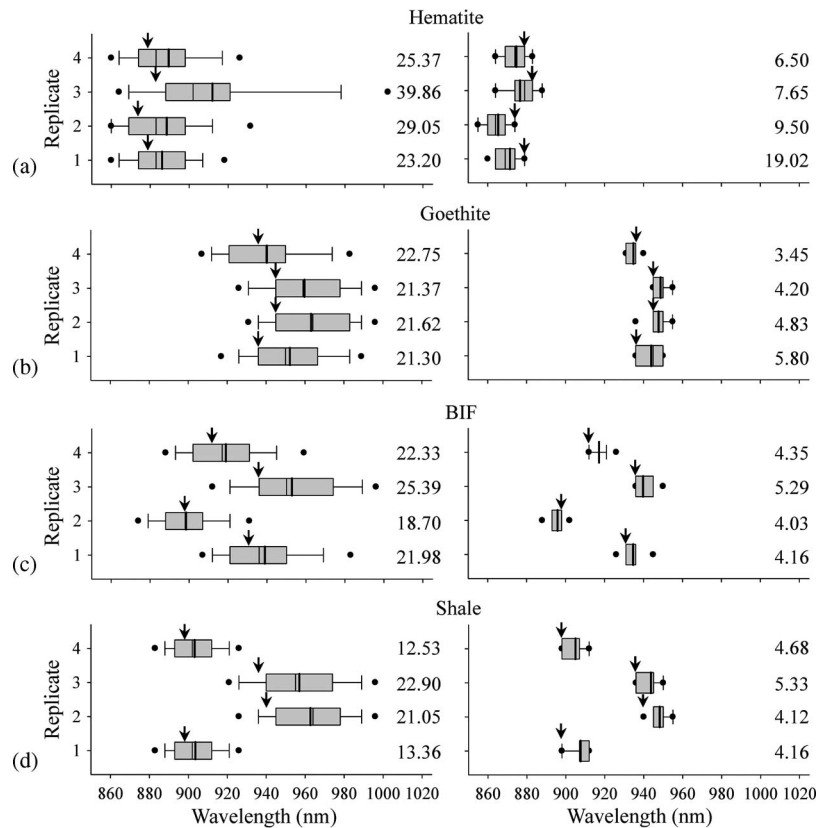
Fig. 3. Variability of the wavelength position of F_{900} for replicate samples of (a) hematite, (b) goethite, (c) BIF, and (d) shale, derived from (left panel) the original data and (right panel) a polynomial fit to the original data. Graphical elements of the box plots describe various statistical attributes of the data: Box boundaries (25th and 95th percentiles), thin and bold lines bisecting box (median and mean of data, respectively), whiskers (10th and 90th percentiles), and filled circles (5th and 95th percentiles of the outliers). The arrows indicate the "true" wavelength position of F_{900}, derived from ASD spectra. Standard deviation is given to the right of each replicate.

inspection. This was done using a magnifying glass to closely examine the color and grain size of the rock surface. Maps were made of the observed distribution of the minerals using measurements of distance between topographical–morphological features on the rock surface. Using these maps together with the original hyperspectral image, separate regions of interest (ROIs) were specified for areas of hematite and goethite, respectively (two ROIs in total). These ROIs were then considered to represent the true "observed" distributions of hematite and goethite on the rock surfaces. Areas which appeared to be composed of mixtures of hematite and goethite were not considered for further analysis and were not included in the ROI.

Because hematite and goethite were present in discrete patches (pixels were likely to be either hematite or goethite and not mixtures thereof), statistical measures used to describe the consistency (i.e., agreement) between the observed distribution and the distribution derived from the wavelength position of F_{900} should operate on categorical, rather than continuous, data. Pixels were therefore classified as hematite or goethite depending on whether the wavelength position of F_{900} was, respectively, below or above a threshold wavelength. This was repeated across a continuum of wavelengths between 820 and 980 nm at intervals of 1 nm. The agreement between the distribution of hematite and goethite mapped by each threshold and their observed distributions (defined by the ROI) were evaluated using the Kappa coefficient of agreement (Kappa) [23], [24] and the receiver operating characteristic (ROC) [25].

TABLE IV
AVERAGE DIFFERENCE (IN NANOMETERS) AMONG REPLICATES ($n = 4$) OF THE WAVELENGTH POSITION OF F_{900} DETERMINED RESPECTIVELY FROM ASD AND IMAGE SPECTRA OF POWDERED ROCK SAMPLES (EXPERIMENT 1)

	Hematite	Goethite	BIF	Shale
Difference (no-p)	-15	-13	-8	-14
Difference (p)	7	-3	-3	-8
Range (no-p)	22	14	17	18
Range (p)	4	9	7	3

Average difference between ASD spectra and original image spectra (no-p). Average difference between ASD spectra and a fifth-order polynomial curve fitted to the original image spectrum (p). Positive and negative values indicate that F_{900} from image spectra have been shifted respectively to shorter and longer wavelengths relative to the ASD spectra. Range is the maximal spectral range (in nanometers) among replicates of rock-powders of the same type.

3) Experiment 3— Wavelength Position of F_{900} as an Indicator of the Proportion of Goethite: With increasing proportion of goethite, the wavelength position of F_{900} shifts to longer wavelengths. The broader spectral bands of the image data and increased amounts of noise may compromise our ability to resolve subtle shifts in wavelength position which occur as a result of small to moderate changes in the proportion of goethite. We tested the hypothesis that relatively small changes
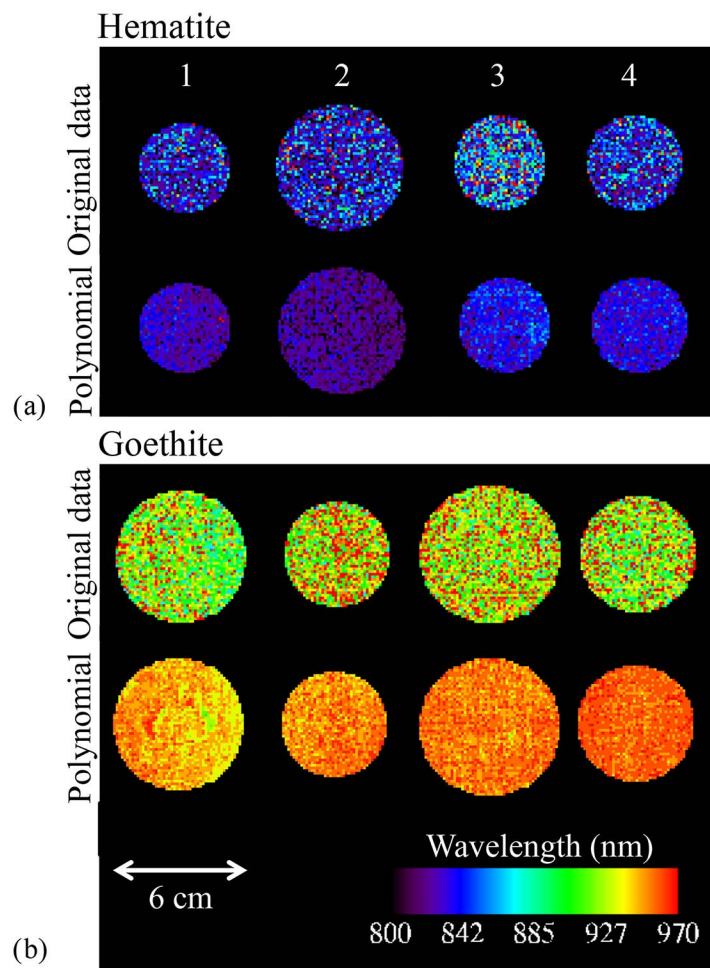
This article has been accepted for inclusion in a future issue of this journal. Content is final as presented, with the exception of pagination.

MURPHY *et al.*: CONSISTENCY OF MEASUREMENTS OF WAVELENGTH POSITION FROM HYPERSPECTRAL IMAGERY 7

Fig. 4. Images of wavelength position of F_{900} for homogeneous powders for each of the four replicate samples of (a) hematite and (b) goethite, derived from the original data and fitted polynomial. The sample replicate number is shown at the top. See also Fig. 3.

in the proportion of goethite can be detected as shifts in the wavelength position of F_{900} derived from hyperspectral imagery. Results were compared with those from ASD spectra.

Independent samples of crushed rock, with particle sizes ranging between 0.2 and 3 mm, were mixed together in an industrial mixer to give variable proportional amounts of goethite relative to hematite (see Table III). Mixtures were placed into separate plastic trays to a depth of 1.75 cm so that the surface was level with the edge of the trays. Eight spatially independent ASD spectra were acquired by randomly placing the reflectance probe on to the surface of each mixture. A hyperspectral image was then acquired of all trays in a single scan.

Pixel values were extracted from the grayscale images representing the wavelength position of F_{900}. To allow the direct comparison of results from the ASD spectrometer and hyperspectral imagery, pixels were extracted from the same areas of sample from which ASD spectra had been previously acquired. To do this, ROIs were specified for each area separately, using an RGB color composite of the hyperspectral image. ROIs were positioned using the faint impressions left on the sample by the outside edge of the reflectance probe as a guide. Pixel values within each ROI were averaged to give eight measurements per mixture (48 measurements in total). These averaged measurements were used for all further analyses.

The strength and nature of the relationship between the wavelength position of F_{900} and the proportion of goethite was explored using analyses of regression. Analysis of variance (ANOVA) was used to test for differences in the wavelength position of F_{900} among mixtures (with six levels and $n = 8$).

4) Experiment 4— Mapping Proportion of Goethite in Rocks on a Vertical Mine Face: Experiment 4 tests the hypothesis that the wavelength position of F_{900} can be determined with sufficient resolution to detect and map spatial variations in the distribution of hematite and goethite on a vertical mine face. In imagery acquired under natural sunlight, atmospheric absorption can significantly increase noise in certain parts of the spectrum, making the determination of wavelength position more challenging. There are four atmospheric absorption features which may increase noise over the spectral region of F_{900}: weak absorptions at 720 and 822 nm, intense features centered on 945 and 1135 nm, and an intense but narrow feature at 762 nm, caused by absorption by oxygen and water vapor (see Fig. 1). Other sensor-induced and environmentally induced factors can also increase noise in data acquired in the field.

Hyperspectral imagery was acquired from a mine face in an open-pit mine at Tom Price, in the Pilbara, Western Australia, during the late Austral springtime. Imagery was collected from a mine face dominated by high-grade ore, principally hematite.
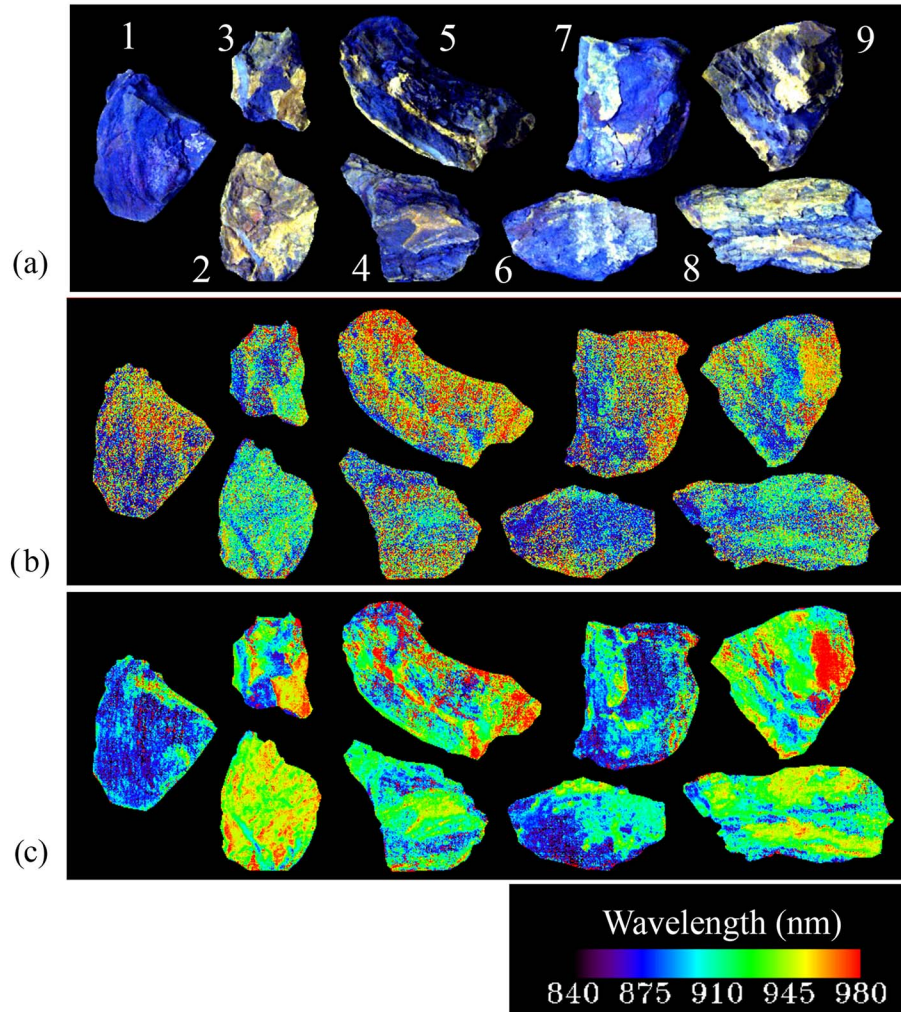
This article has been accepted for inclusion in a future issue of this journal. Content is final as presented, with the exception of pagination.

8

IEEE TRANSACTIONS ON GEOSCIENCE AND REMOTE SENSING

Fig. 5. Wavelength position of F_{900} derived from imagery of whole-rock samples of iron ore composed of hematite and goethite. (a) Contrast enhanced true-color (RGB) composite is shown for context. Patches of hematite are blue, and goethite is yellow cream. Rocks 1 and 2 are composed almost entirely of hematite or goethite, respectively, and all other rocks have variable amounts of hematite or goethite arranged in discrete patches on their surfaces. (b) Wavelength position of F_{900} from original image data. (c) Wavelength of F_{900} derived from a fifth-order polynomial fit to the original data. The color table applied to images in (b) and (c) shows increases in wavelength position as transitions from blue to red.

Rocks, which appeared to be dominantly composed of goethite, were located in isolated patches on the mine face. Quadrats (70 cm × 70 cm) were placed over areas identified, by visual inspection, as hematite or goethite (1 quadrat per area). For validation, between three and five representative rock samples, from within each quadrat, were collected for quantitative XRD analysis.

F. XRD Analysis

XRD analyses were done to provide quantitative information on the abundance of hematite and goethite in samples [26], [27]. Samples were powdered in a ring mill and then micronized with a zinc oxide internal standard for quality control. Diffraction patterns were measured in a PANalytical X'Pert Pro PW3040 diffractometer, fitted with a cobalt tube to provide the source of radiation. Quantitative analysis was done on the diffraction patterns using the SIROQUANT (V3) software developed by the Commonwealth Scientific and Industrial Research Organization (CSIRO).

III. RESULTS

A. Determination of Wavelength Position of F_{900}

Example ASD spectra showed that hematite had a lower reflectance (typically $< 15\%$) compared with goethite [see Fig. 2(a)]. Due to its low reflectance, the image spectra of hematite were noisier than those of goethite. Hematite therefore was used to illustrate the differences between the order of the polynomial and the goodness of fit. The fifth-order polynomial provided a better fit to the data than did the fourth-order one (see Fig. 2). Differences were found in the wavelength position of F_{900} derived from the fourth- and fifth-order polynomials, with the fifth-order polynomial being closer to the "true" wavelength position determined from ASD spectra [see Fig. 2(d)].

B. Experiment 1: Consistency of Wavelength Position of F_{900} in Homogeneous Samples

Variability in the wavelength position of F_{900} derived from the original data and from the polynomial fit was compared using all pixels in each sample (see Fig. 3). Large amounts of

variability were observed in the wavelength position of F_{900} derived from the original data, causing some pixel values from hematite to overlap with those of goethite. In comparison, the variability in the wavelength position of F_{900} derived from a polynomial fit was much smaller, and there was a large interval of wavelengths (45 nm) between maximal values for hematite and minimal values for goethite [cf. Fig. 3(a) and (b)]. Similar amounts of variability were observed for BIF and shale which tended to have weaker absorption features than did goethite. Differences between the "true" wavelength position of F_{900}, derived from ASD spectra (shown by arrows), and the average wavelength position of pixel spectra over the entire sample (shown by the bold line bisecting each box) are much greater for F_{900} derived from the original data compared with the fitted polynomial (see Fig. 3 and Table IV). Large shifts of F_{900} to longer wavelengths were found when it was derived from the original data (see Fig. 3 and Table IV). This positive bias in wavelength degraded the spatial consistency of pixels representing the wavelength position within each homogeneous sample. Compare, for example, the spatial variability in the wavelength position of F_{900} for replicate 3 of hematite derived from the original data and the fitted polynomial (see Fig. 4).

C. Experiment 2: Consistency of Wavelength Position of F_{900} in Whole-Rock Samples

An enhanced true-color composite shows the approximate distribution of hematite and goethite in the rock samples [see Fig. 5(a)]. The image of the wavelength position of F_{900}, derived from the original data, showed large amounts of spatial variability among pixels [see Fig. 5(b)]. The wavelength position of F_{900} in some areas of some samples (e.g., the top of Sample 1) was shifted to longer wavelengths (i.e., > 930 nm) than would be expected from its composition. This sample was composed almost entirely of hematite, yet the wavelength position of F_{900} from pixels in the topmost area indicated goethite (i.e., their wavelengths tended toward those of goethite; see results from [15] in Table I). The reverse situation is found for Sample 2 (composed almost entirely of goethite), yet many pixels had wavelengths consistent with hematite (blue image tones). The image of the wavelength position of F_{900} derived from the polynomial fit showed less spatial variability [see Fig. 5(c)]. Samples 1 and 2 had wavelengths which were largely consistent with their dominant composition (hematite or goethite, respectively).

Values representing the wavelength position of F_{900} were extracted from the images, separately for each of the ROI describing the true distribution of hematite and goethite. From these data, histograms showed that the wavelength position of F_{900}, derived from the original image, had overlapping distributions for hematite and goethite [see Fig. 6(a)]. This indicated that F_{900} derived from these data did not describe the observed spatial distribution of either hematite or goethite. The histogram of the wavelength position of F_{900}, derived from a polynomial fit to the original data, showed a bimodal distribution. The distribution of hematite (peak frequency at 881 nm) was distinctly different to goethite [peak frequency at 932 nm; see Fig. 6(b)]. This indicated that the wavelength
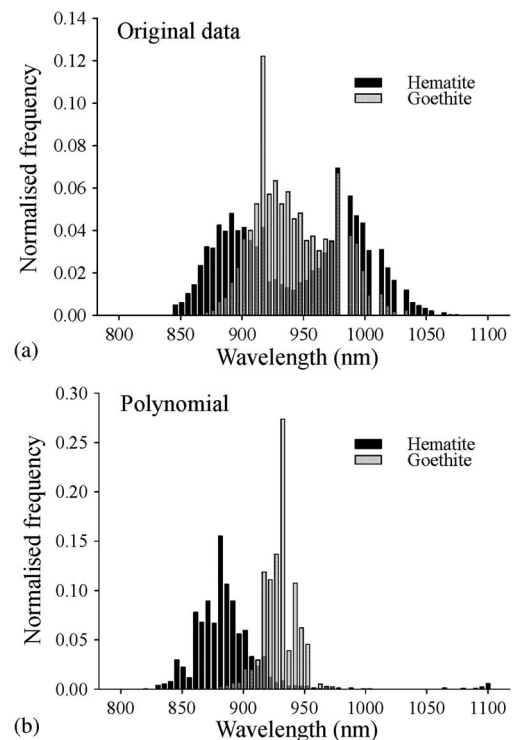

Fig. 6. Frequency distributions of the wavelength position of F_{900} from whole-rock samples (Experiment 2), normalized to the number of pixels in each ROI representing hematite or goethite. (a) F_{900} derived from the original data. (b) F_{900} derived from a polynomial fit to the original data.

position of F_{900}, derived from a polynomial fit of the original image data, was consistent with the observed distributions of hematite and goethite. The small overlap between the modal distributions was probably caused by pixels composed of mixtures of hematite and goethite.

The Kappa coefficient showed that there was very poor or no agreement $(\text{Kappa} = 0.1)$ between the observed distribution of hematite and goethite and the wavelength position of F_{900} derived from the original data [see Fig. 7(a)]. Conversely, the highest values of Kappa (peak > 0.68) indicated that there was a very good agreement between the observed distribution of hematite and goethite and the wavelength position of F_{900} derived from a polynomial fit to the original data. The threshold wavelength which provided the optimal separation of hematite and goethite was 902 nm [see Fig. 7(a)]. ROC curves indicated that, across all threshold values used, the wavelength position derived from the fitted polynomial was consistently better at describing the observed distribution of hematite and goethite than the wavelength position derived from the original data [see Fig. 7(b)].

D. Experiment 3: Wavelength Position of F_{900} as an Indicator of the Proportion of Goethite

Continuum-removed spectra (770–1150 nm) of individual pixels from the original imagery and the polynomial fit are shown in Fig. 8. Most spectra of mixtures from the original image showed a marked increase in noise at wavelengths greater than 930 nm, making it difficult to identify any coherent
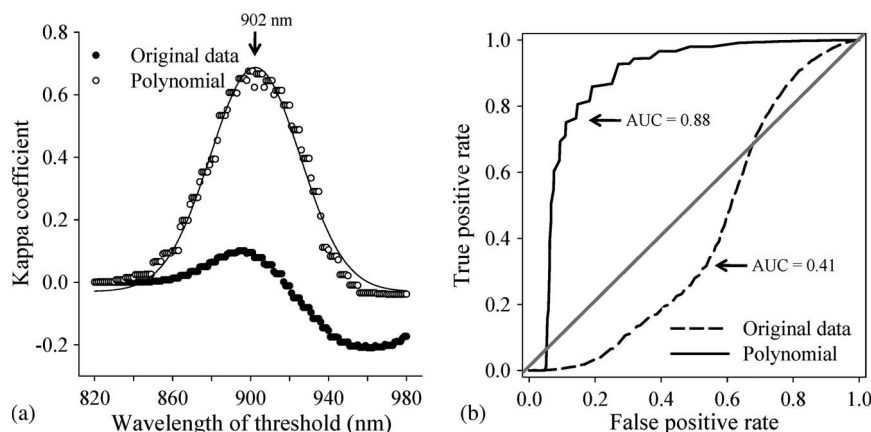
This article has been accepted for inclusion in a future issue of this journal. Content is final as presented, with the exception of pagination.

10   IEEE TRANSACTIONS ON GEOSCIENCE AND REMOTE SENSING

Fig. 7.   (a) Kappa coefficient of agreement between observed and predicted distributions of hematite and goethite mapped using a threshold of the wavelength position of F_{900}. The threshold wavelength started at 820 nm and was incremented by 1 nm until it reached 980 nm. Pixels with a wavelength below and above the threshold were classified as hematite and goethite, respectively. A fitted curve which best describes Kappa values derived from the polynomial fit is shown (solid line). The threshold wavelength which provided the optimal separation between hematite and goethite (i.e., the peak of the fitted curve) is indicated by the arrow. (b) ROC curves showing the overall agreement between observed distribution of hematite and goethite and that mapped by wavelength position derived from the original data and polynomial fit. The area under each curve (AUC) is indicated. The diagonal is the line of random guess $(AUC = 0.5)$.

progressive increase in the wavelength position of F_{900} with increasing proportion of goethite [see Fig. 8(a)]. Spectra of the fitted polynomial show a progressive change in the wavelength position of F_{900} from shorter to longer wavelengths with increasing proportion of goethite [arrow in Fig. 8(b)].

There were strong relationships between the proportion of goethite derived from XRD analysis and the wavelength position of F_{900} (see Fig. 9 and Table V). The strength of the relationships were similar for ASD spectra, the original image data, and the polynomial derived from the original image data (see Fig. 9(a)–(c), respectively). The slope and intercept of the regression line for ASD spectra and the fitted polynomial were similar; however, the intercept for the original data showed a positive bias. This is consistent with the shift in F_{900} to longer wavelengths, found in Experiments 1 and 2, when it was derived from the original image data. Variability among the eight replicates was greatest for F_{900} derived from the original data [note larger error bars in Fig. 9(b)].

There were significant differences in the wavelength position of F_{900} among the artificial mixtures of crushed rock (see Fig. 9 and Table VI). Student–Newman–Keuls (SNK) tests were used to test for significant differences in wavelength position between pairs of mixtures. Two contrasting results were found: 1) The wavelength position of F_{900} derived from the ASD spectra and from the original image showed significant differences among all mixtures of crushed rock, except for the samples with the two smallest proportions of goethite, i.e., Samples 1 and 2 (see Table III); these were not significantly different from one another, but together they were significantly different from all other mixtures [see Fig. 9(a) and (b)]; and 2) the wavelength position of F_{900} derived from the fitted polynomial of the original image was significantly different among all mixtures [see Fig. 9(c)].

E. Experiment 4: Mapping Proportion of Goethite in Rocks on a Vertical Mine Face

The original image of the mine face showed color changes between areas which were thought, from inspection of the rocks
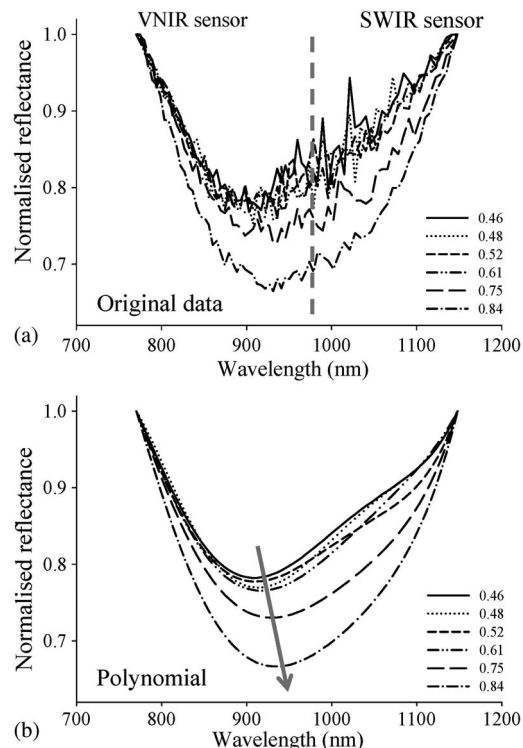

Fig. 8.   Normalized image spectra (770–1150 nm) from a single image pixel, randomly selected from each mixture of crushed rock $(n = 6)$. Figures in legend indicate the proportion of goethite in the sample, derived from XRD: (a) Original data and (b) polynomial fit. The wavelength of the crossover point between the VNIR and SWIR sensors is indicated by the vertical dashed line in (a). The direction of the shift in wavelength position of F_{900} associated with an increase in the proportion of goethite is indicated by the arrow in (b).

in the field, to be either hematite or goethite [see Fig. 10(a)]. The wavelength position of F_{900} derived from the original data showed poor correspondence with the spatial distribution of hematite and goethite identified in the field [cf. Fig. 10(a) and (b)]. In Fig. 10(b), colors representing wavelengths longer than 900 nm are predominant, which indicated, incorrectly, that the dominant mineral on the mine face was goethite, not hematite. In contrast, the wavelength position of F_{900}, derived from a
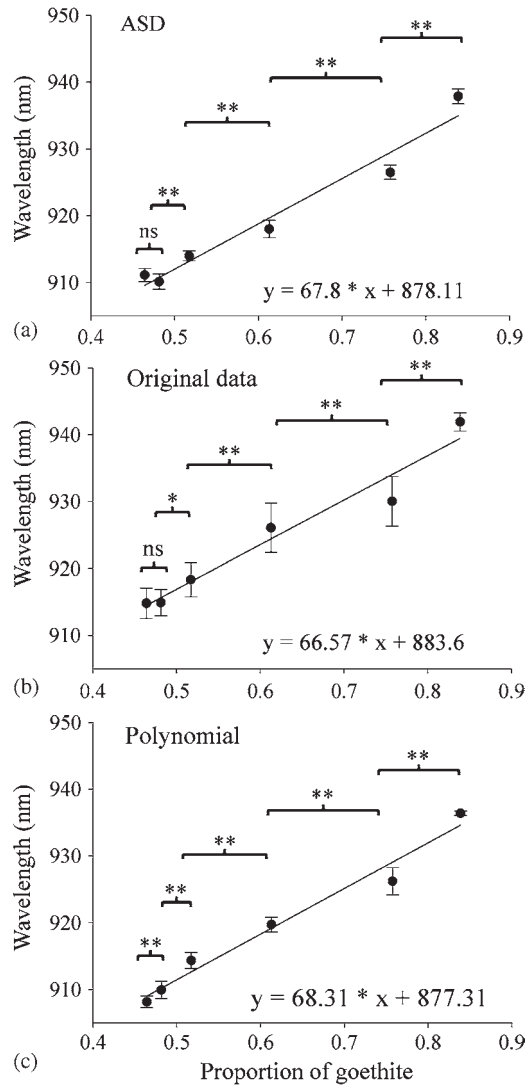
Fig. 9. Wavelength position of F_{900} in ASD and image spectra of artificial mixtures of crushed rock with variable proportions of goethite. (a) ASD spectra. (b) Spectra from original image. (c) Fifth-order polynomial fitted to spectra from original image. Error bars in each case are standard deviation, representing variability among replicates ($n = 8$). Brackets above plot symbols indicate statistical significance of differences in wavelength position between pairs of mixtures (SNK tests): (NS) nonsignificant, ($*$) $P < 0.05$, and ($**$) $P < 0.01$. Equations at the bottom right of each graph are from a regression analysis of wavelength position on the proportion of goethite derived from XRD.

TABLE V
RESULTS FROM LINEAR REGRESSION OF WAVELENGTH POSITION OF THE FERRIC IRON CRYSTAL FIELD ABSORPTION AT $\sim$900 nm ON THE PROPORTION OF GOETHITE ($n = 6$ DIFFERENT PROPORTIONS)

	R^2	SE	P
ASD spectra	0.96	2.42	< 0.001
Image spectra (original data)	0.95	2.53	< 0.001
Image spectra (polynomial)	0.97	1.96	< 0.001

Each data point is the average of eight replicate measurements made by the reflectance probe (ASD spectra) or of pixels within ROIs specified in each sample tray (image spectra). See also Fig. 9.

TABLE VI
ANALYSES (ANOVA; SINGLE FACTOR AND SIX LEVELS) OF MEAN WAVELENGTH POSITION OF F_{900} DERIVED FROM SPECTRA ACQUIRED FROM EACH OF SIX ARTIFICIAL MIXTURES ($n = 8$ REPLICATES FOR EACH MIXTURE)

ASD spectra (no polyn.)

Source	df	MS	F	P
Mixture	5	923.37	797.56	< 0.0001
Residual	42	1.16		

Original image

Source	df	MS	F	P
Mixture	5	895.15	111.49	< 0.0001
Residual	42	8.02		

Polynomial fit

Source	df	MS	F	P
Mixture	5	923.9	559.55	< 0.0001
Residual	42	1.65		

Pairwise SNK tests showed significant differences in wavelength position between mixtures (i.e. levels in the analysis; see Fig. 9).

polynomial fit to the original data, showed broad agreement with the mineral distribution identified in the field [cf. Fig. 10(a) and (c)]. The majority of pixel spectra in the image had a wavelength position of less than 900 nm, consistent with hematite, the dominant mineral on the mine face. Patches of goethite on the mine face had longer wavelengths (i.e., > 900 nm). The wavelength position of F_{900} within each quadrat was shifted to longer wavelengths when derived from the original image data, compared to the polynomial fit (see Fig. 11).

Quantitative XRD analysis showed that, on average, rocks in Q1 contained 97.4 wt% hematite and 0 wt% goethite. Samples from Q2 contained 73 wt% hematite and 21.9 wt% goethite. XRD analyses were therefore consistent with the wavelength position of F_{900} derived from the polynomial fit but not the original imagery.

IV. DISCUSSION

The determination of the wavelength position of F_{900}, as an indicator of mineralogy, has been explored by previous studies using nonimaging hyperspectral data collected mainly under laboratory conditions from discrete areas of rock or from rock chips. Although these studies found strong correlations between wavelength position and some aspects of mineralogy (e.g., the proportion of goethite in samples), it cannot be assumed that these strong correlations could be achieved from image data. Without some knowledge about the variability in wavelength position arising as a consequence of instrument noise or methods of measurement, no conclusions can be drawn from maps of wavelength position determined from image data. Image
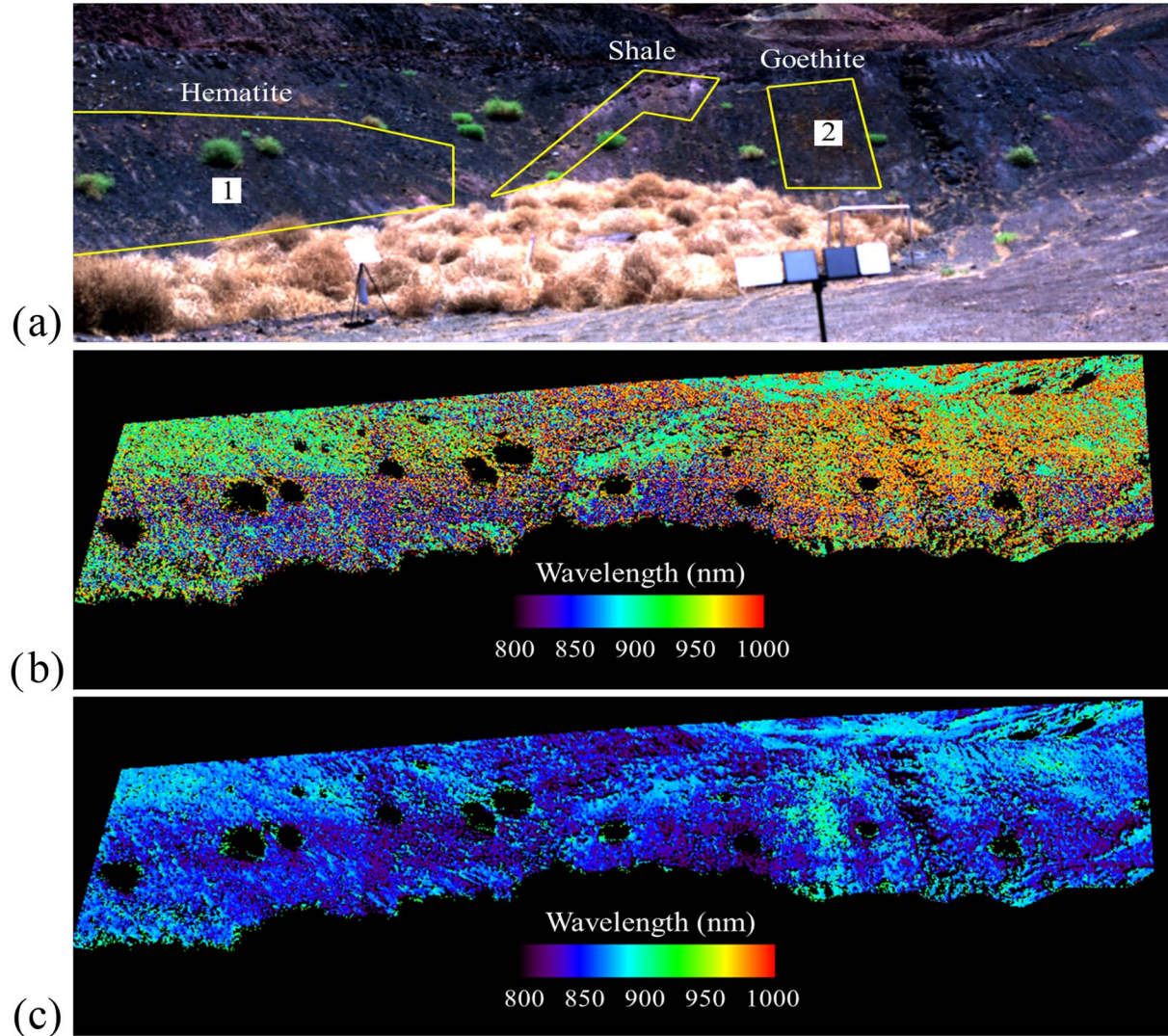
Fig. 10.   Wavelength position of F_{900} derived from imagery of a mine face. (a) True-color composite showing location of the quadrats from where samples were taken (white squares): $1 = $ Hematite, and $2 = $ Goethite. Approximate boundaries of areas mapped in the field as hematite, shale, and goethite are shown (yellow polygons). (b) Wavelength position of F_{900} derived from the original data. (c) Wavelength position of F_{900} derived from a polynomial fit to the original data.

spectra, for the reasons already stated, are typically noisier than spectra acquired by nonimaging instruments, such as the ASD spectrometer. In maps of wavelength position, derived from imagery on a per-pixel basis, noise in the spectral domain has the potential to be translated into the spatial domain, degrading spatial patterns. Thus, spatial variability in wavelength position may be greater than the "true" variability which arises solely from changes in mineralogy. This variability may be large enough to undermine the very basis for using imagery, i.e., to provide spatial context.

Our study examined rigorously the consistency with which wavelength position in the VNIR can be determined from imagery. We selected the ferric iron crystal field absorption—F_{900}—because it provided a difficult test of our ability to extract wavelength position from imagery. Experiment 1 examined variability in the wavelength position of F_{900}, from compositionally homogeneous powders. Because data were acquired under identical conditions of measurement from homogeneous powders with uniform characteristics of reflectance,

there should be little or no variability in the wavelength position of F_{900} for pixels within each sample. This was not the case for the wavelength position derived from the original image data. Pixel values describing the derived wavelength positions within each sample showed large amounts of variability. Large differences were found between mean wavelength positions of pixels within each sample and wavelengths derived from ASD spectra. An unexpected, yet significant, finding was that the wavelength position of F_{900} derived from the original image spectra showed a positive bias compared with that from ASD spectra (i.e., a shift to longer wavelengths, particularly in spectra with low albedo). The reason for this was that image data beyond 930 nm became progressively noisier as the sensitivity of the VNIR sensor decreased. Noise was further amplified by the procedure (arithmetic division) used to remove the spectral continuum. Noise also increased the apparent depth of the absorption feature, thus increasing the likelihood that a minimum will be "found" in the noisiest parts of the spectrum. These effects can be illustrated with reference to the wavelength

position of the smallest value in the original image spectrum (i.e., the nominal wavelength position of F_{900} [see gray lines in Fig. 2(c) and (d)]. Prior to the removal of the continuum, the wavelength position of F_{900} is 880 nm [see Fig. 2(c)], but after normalization, the wavelength position is 985 nm—a shift of 105 nm to longer wavelengths [see Fig. 2(d)]. Deriving the wavelength position from a polynomial fitted to the original data substantially reduced variability and reduced the differences in mean wavelength position between the image and ASD spectra. The positive bias in wavelength position was also largely removed. Using this approach, patches of hematite and goethite on samples of whole rock and on the mine face could be mapped using wavelength position.

The ability to determine accurately the amount of goethite, as a proportion of the total amount of iron minerals, has economic significance because, for some deposits of iron ore, it may be used as a factor in determining the grade of ore. This has also important implications for the processing of iron ore as large amounts of goethite can have adverse effects on machinery. Few, if any, published studies have used hyperspectral imagery to quantify the wavelength position of F_{900} from imagery acquired from field-based platforms. In order to compare directly the image and ASD spectra, our analyses used wavelength positions derived on a per-pixel basis from the original data. These values were then integrated (averaged) over the area measured by the reflectance probe used to acquire ASD spectra. Spatial averaging of pixels reduced variability in the wavelength position caused by noise in the spectral domain but not the positive bias. Thus, the wavelength positions of F_{900} derived from the original image data and ASD spectra showed similar strong correlations, but the former had a larger intercept caused by the positive bias (see Fig. 9). To standardize measurements across studies, data sets, or instruments, it is evident therefore that the wavelength position of F_{900} should be derived using a consistent method, specifically by using the same end points (wavelengths) for the removal of the continuum and the same order of the polynomial.

Smoothing of the data using spectral filters may also be effective in reducing noise in the data, but this is unlikely to be as effective as a polynomial fit. This is because noise in some parts of the VNIR spectrum, e.g., at the joining point between the sensors and at the location of atmospheric absorptions, is often superimposed on a positive or negative shift in reflectance which may be maintained consistently over several wavelengths. Such noise is difficult to isolate and remove, even using more sophisticated filtering techniques (e.g., [18] and [28]). The shift in reflectance at the boundary of the imaging sensors could potentially be reduced by using advanced automated methods to spatially register the VNIR and SWIR components of the data cube (e.g., [29]), although this has yet to be demonstrated experimentally.

Wavelength position was used in this study as a continuous variable to estimate the proportion of goethite in samples and as a categorical measure of the ore type. The latter approach may be especially useful in the context of mapping mineralogy. Vertical mine faces exhibit large variations in incident illumination. Many established methods of classification (e.g., SAM) classify spectra of unknown identity by comparing their
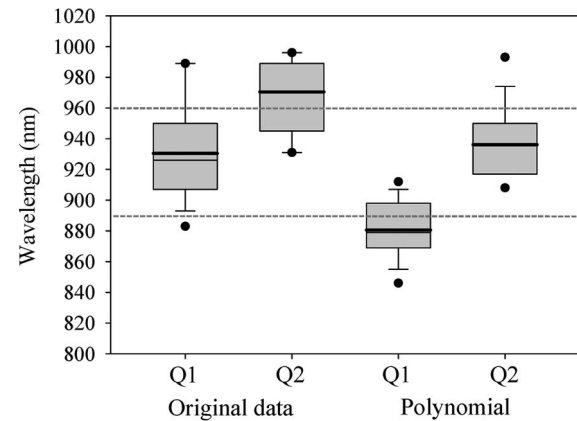

Fig. 11. Variability in wavelength position of F_{900} generated from the original data and from the polynomial fit. Data are from pixels within each quadrat (see Fig. 10). Q1 = hematite, and Q2 = goethite. The horizontal dashed lines are the approximate upper and lower wavelength boundaries of F_{900} found by Haest *et al.* [15] (see Table I). For a complete description of the graphical elements comprising the box plots, see Fig. 3 (caption).

spectral curve shape with a library of known mineral spectra. Because SAM is an angular measure, it is relatively insensitive to variations in the brightness of spectra [30], [31]. This reduces its effectiveness in distinguishing hematite and goethite because, after scaling their spectra to similar brightness, their spectral curve shapes between 400 and 2450 nm are similar. The major difference between these spectra is that they have very different brightness. Brightness cannot be exploited as a method of classification for imagery of mine faces because the large variations in incident illumination would mask differences in reflectance due to their intrinsic properties of reflectance [32]. Our results show that hematite and goethite can be classified using a simple threshold of the wavelength position of F_{900} at 902 nm. This presents a way of classifying these minerals without relying on an angular metric or differences in brightness which, for the aforementioned reasons, could be ineffective. Further work, however, needs to be done to confirm that the wavelength position of F_{900} is insensitive to variations in incident illumination.

The increasing use of hyperspectral imagery acquired in field settings continues to open up new applications for its use. The experiments described here provide the first validated results which show that the wavelength position of absorption features in the VNIR can be determined from hyperspectral imagery acquired in the laboratory and in the field. Further work is underway to improve the accuracy and precision with which the wavelength position of absorption features can be determined from image spectra using machine learning techniques.

V. Conclusion

The determination of wavelength position of absorption features in the VNIR (400–1200 nm) from hyperspectral imagery is more challenging than that for data acquired using non-imaging instruments. The wavelength position of absorption features, such as those of ferric iron minerals which straddle the spectral regions sampled by different sensors, cannot be reliably extracted directly from hyperspectral imagery. Spectral

noise caused a shift in the wavelength position of the ferric iron feature to longer wavelengths, making it impossible to map distributions of hematite and goethite, even from imagery acquired under ideal conditions in the laboratory. Conversely, wavelength position determined from a polynomial fit to the image pixel spectra enabled the spatial distributions of hematite and goethite to be mapped from laboratory imagery of rock samples and from field imagery of a vertical mine wall. Thus, the wavelength position, as a feature, can be used as a categorical measure of the distribution of iron minerals. The use of wavelength position derived from hyperspectral imagery to quantify the proportion of goethite in samples is demonstrated. The overarching conclusion of these studies is that the wavelength position of features in the VNIR (400–1200 nm) should be determined from imagery using a polynomial (or equivalent) fit to the data and not from the original data themselves.

Acknowledgment

References

[1] A. F. H. Goetz, "Three decades of hyperspectral remote sensing of the Earth: A personal view," *Remote Sens. Environ.*, vol. 113, no. S1, pp. S5–S16, Sep. 2009.

[2] A. Plaza, J. A. Benediktsson, J. W. Boardman, J. Brazile, L. Bruzzone, G. Camps-Valls, J. Chanussot, M. Fauvel, P. Gamba, A. Gualtieri, M. Marconcini, J. C. Tilton, and G. Trianni, "Recent advances in techniques for hyperspectral image processing," *Remote Sens. Environ.*, vol. 113, no. S1, pp. S110–S122, Sep. 2009.

[3] E. A. Cloutis, "Hyperspectral geological remote sensing: Evaluation of analytical techniques," *Int. J. Remote Sens.*, vol. 17, no. 12, pp. 2215–2242, Aug. 1996.

[4] F. A. Kruse, A. B. Lefkoff, J. W. Boardman, K. B. Heidebrecht, A. T. Shapiro, P. J. Barloon, and A. F. H. Goetz, "The Spectral Image Processing System (SIPS)—Interactive visualization and analysis of imaging spectrometer data," *Remote Sens. Environ.*, vol. 44, no. 2/3, pp. 145–163, May/Jun. 1993.

[5] J. J. Settle and N. A. Drake, "Linear mixing and the estimation of ground cover proportions," *Int. J. Remote Sens.*, vol. 14, no. 6, pp. 1159–1177, Apr. 1993.

[6] J. Luis Silvan-Cardenas and L. Wang, "Fully constrained linear spectral unmixing: Analytic solution using fuzzy sets," *IEEE Trans. Geosci. Remote Sens.*, vol. 48, no. 11, pp. 3992–4002, Nov. 2010.

[7] S. Schneider, A. Melkumyan, R. J. Murphy, and E. Nettleton, "Gaussian processes with OAD covariance function for hyperspectral data classification," in *Proc. 22nd IEEE Int. Conf. Tools Artif. Intell.*, Arras, France, 2010, pp. 393–400.

[8] J. K. Crowley, D. E. Williams, J. M. Hammarstrom, N. Piatak, I. M. Chou, and J. C. Mars, "Spectral reflectance properties (0.4–2.5 μm) of secondary Fe-oxide, Fe-hydroxide, and Fe-sulphate-hydrate minerals associated with sulphide-bearing mine wastes," *Geochem. Explor. Environ. Anal.*, vol. 3, no. 3, pp. 219–228, Aug. 2003.

[9] R. V. Morris, H. V. Lauer, Jr., C. A. Lawson, E. K. Morris, Jr., G. A. Nace, and C. Stewart, "Spectral and other physicochemical properties of submicron powders of hematite ($\alpha - Fe_2O_3$), maghemite ($\gamma - Fe_2O_3$), magnetite (Fe_3O_4), goethite (α-FeOOH), and lepidocrocite (γ-FeOOH)," *J. Geophys. Res.*, vol. 90, no. B4, pp. 3126–3144, Mar. 1985.

[10] A. C. Scheinost, D. G. Schulze, and U. Schwertmann, "Diffuse reflectance spectra of Al substituted goethite: A ligand field approach," *Clays Clay Minerals*, vol. 47, no. 2, pp. 156–164, Apr. 1999.

[11] F. A. Kruse, "Use of airborne imaging spectrometer data to map minerals associated with hydrothermally altered rocks in the northern grapevine mountains, Nevada, and California," *Remote Sens. Environ.*, vol. 24, no. 1, pp. 31–51, Feb. 1988.

[12] R. N. Clark, V. V. Trude, T. V. V. King, M. Klejwa, G. A. Swayze, and V. Norma, "High spectral resolution reflectance spectroscopy of minerals," *J. Geophys. Res.*, vol. 95, no. B8, pp. 12 653–12 680, Aug. 1990.

[13] R. J. Murphy, "The effects of surficial vegetation cover on mineral absorption feature parameters," *Int. J. Remote Sens.*, vol. 16, no. 12, pp. 2153–2164, Aug. 1995.

[14] F. T. Barranco, W. L. Balsam, and B. C. Deaton, "Quantitative reassessment of brick red lutites—Evidence from reflectance spectrophotometry," *Marine Geol.*, vol. 89, no. 3/4, pp. 299–314, Oct. 1989.

[15] M. Haest, T. Cudahy, C. Laukamp, and S. Gregory, "Quantitative mineralogy from infrared spectroscopic data. I. Validation of mineral abundance and composition scripts at the Rocklea Channel iron deposit in Western Australia," *Econom. Geol.*, vol. 107, no. 2, pp. 209–228, Apr. 2012.

[16] V. M. Sellitto, R. B. A. Fernandes, V. Barrón, and C. Colombo, "Comparing two different spectroscopic techniques for the characterization of soil iron oxides: Diffuse versus bi-directional reflectance," *Geoderma*, vol. 149, no. 1/2, pp. 2–9, Feb. 2009.

[17] T. J. Cudahy and E. R. Ramanaidou, "Measurement of the hematite: Goethite ratio using field visible and near-infrared reflectance spectrometry in channel iron deposits, western Australia," *Australian J. Earth Sci.*, vol. 44, no. 4, pp. 411–420, Aug. 1997.

[18] A. Melkumyan and R. Murphy, "Spectral domain noise suppression in dual-sensor hyperspectral imagery using Gaussian processes," in *Neural Information Processing. Models and Applications*, vol. 6444, K. Wong, S. U. Mendis, and A. Bouzerdoum, Eds. Berlin/Heidelberg, Germany: Springer-Verlag, 2010, pp. 684–691.

[19] E. Ramanaidou, M. Wells, D. Belton, M. Verrall, and C. Ryan, "Mineralogical and microchemical methods for the characterization of high-grade banded iron formation-derived iron ore," in *Reviews in Economic Geology: Banded Iron Formation-Related High-Grade Iron Ore*, vol. 15, S. Hagemann, C. A. Rosiere, J. Gutzmer, and N. Beukes, Eds. Westminster, CO, USA: Society of Economic Geologists, 2008, pp. 129–156.

[20] A. Savitzky and M. J. E. Golay, "Smoothing and differentiation of data by simplified least squares procedures," *Anal. Chem.*, vol. 36, no. 8, pp. 1627–1639, Jul. 1964.

[21] R. J. Murphy, "Mapping of jasperoid in the Cedar Mountains, Utah, U.S.A., using imaging spectrometer data," *Int. J. Remote Sens.*, vol. 16, no. 1, pp. 1021–1041, Jan. 1995.

[22] R. N. Clark and T. L. Roush, "Reflectance spectroscopy: Quantitative analysis techniques for remote sensing applications," *J. Geophys. Res.*, vol. 89, no. B7, pp. 6329–6340, Jul. 1984.

[23] R. G. Congalton, R. G. Oderwald, and R. A. Mead, "Assessing Landsat classification accuracy using discrete multivariate-analysis statistical techniques," *Photogramm. Eng. Remote Sens.*, vol. 49, no. 12, pp. 1671–1678, Jan. 1983.

[24] W. D. Hudson and C. W. Ramm, "Correct formulation of the Kappa coefficient of agreement," *Photogramm. Eng. Remote Sens.*, vol. 53, no. 4, pp. 421–422, Apr. 1987.

[25] T. Fawcett, "An introduction to ROC analysis," *Pattern Recognit. Lett.*, vol. 27, no. 8, pp. 861–874, Jun. 2006.

[26] D. G. Schulze, "Identification of soil iron-oxide minerals by differential X-ray-diffraction," *Soil Sci. Soc. Amer. J.*, vol. 45, no. 2, pp. 437–440, Mar. 1981.

[27] U. Schwertmann and R. M. Taylor, "Iron oxides," in *Minerals in Soil Environments*, J. B. Dixon and S. B. Weed, Eds. Madison, WI: Soil Science Society of America, 1989, pp. 379–438.

[28] R. L. Huguenin and J. L. Jones, "Intelligent information extraction from reflectance spectra: Absorption band positions," *J. Geophys. Res.*, vol. 91, no. B9, pp. 9585–9598, Aug. 1986.

[29] Z. Taylor and J. Nieto, "A mutual information approach to automatic calibration of camera and lidar in natural environments," in *Proc. ACRA*, Wellington, New Zealand, 2012, pp. 1–8.

[30] C. Hecker, M. van der Meijde, H. van der Werff, and F. D. van der Meer, "Assessing the influence of reference spectra on synthetic SAM classification results," *IEEE Trans. Geosci. Remote Sens.*, vol. 46, no. 12, pp. 4162–4172, Dec. 2008.

[31] F. Van der Meer, "The effectiveness of spectral similarity measures for the analysis of hyperspectral imagery," *Int. J. Appl. Earth Observ. Geoinf.*, vol. 8, no. 1, pp. 3–17, Feb. 2006.

[32] R. J. Murphy, S. T. Monteiro, and S. Schneider, "Evaluating classification techniques for mapping vertical geology using field-based hyperspectral

sensors," *IEEE Trans. Geosci. Remote Sens.*, vol. 50, no. 8, pp. 3066–3080, Aug. 2012.

[33] T. E. Townsend, "Discrimination of iron alteration minerals in visible and near-infrared reflectance data," *J. Geophys. Res.*, vol. 92, no. B2, pp. 1441–1454, Feb. 1987.

[34] W. F. Buckingham and S. E. Sommer, "Mineralogical characterization of rock surfaces formed by hydrothermal alteration and weathering—Application to remote-sensing," *Econom. Geol.*, vol. 78, no. 4, pp. 664–674, Jul. 1983.

Richard J. Murphy (M'12) received the B.Sc. degree from University College London, London, U.K., in 1988 and the Ph.D. degree from the University of Reading, Berkshire, U.K., in 1993.

At the University of Reading, his research was on the effects of vegetation on the hyperspectral signature of soils and minerals. At Plymouth Marine Laboratory, Plymouth, U.K., his contribution to the Land–Ocean Interaction Study (LOIS), from 1993 to 1995, was to develop algorithms to derive measures of water quality from remotely sensed data of coasts and estuaries. Appointed to the position of Scientist with the National Institute of Water and Atmosphere, New Zealand, he developed and led New Zealand's Ocean Colour Programme, from 1995 to 1999. He is currently a Senior Research Fellow with The University of Sydney, Sydney, Australia, where he has developed multispectral and spectroscopic methods for quantifying and characterizing intertidal biofilms *in situ*. His current work at the Australian Centre for Field Robotics, The University of Sydney, involves the use of field-based sensors for geological applications.

Dr. Murphy is a member of the IEEE Geoscience and Remote Sensing Society.

Sven Schneider received the Diplom-Engineer degree in photonics and image processing from the University of Applied Sciences, Darmstadt, Germany, in 2008. He is currently working toward the Ph.D. degree at the Australian Centre for Field Robotics, The University of Sydney, Sydney, Australia.

He joined the Australian Centre for Field Robotics in 2009, as an Engineer for hardware and software development. His field of research is the classification of hyperspectral data using machine learning. His research interests include pattern recognition, remote sensing, multi/hyperspectral image processing, and medical imaging.

Sildomar T. Monteiro (M'06) received the M.Sc. degree in computer science from the Aeronautics Technological Institute, Sao Jose dos Campos, Brazil, in 2002 and the Ph.D. degree in engineering from the Tokyo Institute of Technology, Tokyo, Japan, in 2007.

From 2008 to 2013, he was a Research Fellow with the Australian Centre for Field Robotics, The University of Sydney, Sydney, Australia. In August 2013, he will join the Rochester Institute of Technology, Rochester, NY, USA, as an Assistant Professor with the Department of Electrical and Microelectronic Engineering. His research interests include machine learning, statistical signal and image processing, and their applications, particularly in robotics, remote sensing, and biomedical engineering.

Dr. Monteiro is a member of the Association for Computing Machinery. He serves as a Guest Editor of the *Journal of Field Robotics* special issue on Alternative Sensing Techniques for Robot Perception, 2013. He was the recipient of a Japan Society for the Promotion of Science Postdoctoral Fellowship in 2007.